Penta carbides: Two-dimensional group-IV semiconductors containing C$_2$ dimers for nanoelectronics and photocatalytic water splitting

Mehmet Emin Kilic[*] and Kwang-Ryeol Lee[†]

Computational Science Center, Korea Institute of Science and Technology, Seoul 136-791, Republic of Korea

The discovery of novel materials with superior tailored properties is highly attractive for nano- and optoelectronics. Inspired by penta graphene, we introduce a novel family of two-dimensional group-IV materials with C$_2$ dimers, namely penta carbides. The first-principles calculations reveal that the unitary, binary, and ternary penta carbides have excellent energetic, dynamical, thermal, and mechanical stability with remarkable properties. The unitary penta carbide displays auxetic behavior whereas the binary and ternary penta carbides posses near zero and positive Poisson's ratio. The phonon dispersion curves of penta carbides indicate a remarkable phononic gap, which can be tuned by alloy engineering and hydrogenation. They are semiconductor in nature with band-gap energy ranging from 1.35 and 2.39 eV. Alloying and strain engineering enable the direct modification of atomic bonding and thereby tuning of electronic band gap of penta carbides. Such novel tunable electronic and phononic properties of penta carbides can find applications in the field of nanoelectronics, sensors, and frequency filter applications. The band edge positions of penta carbides (except for Sn-based ones) straddle the redox potentials of water. Remarkably, penta carbides exhibit very high optical absorption in the visible and ultraviolet regions (up to 10^{-6} cm^{-1}). They have small and anisotropic carrier effective masses, indicating fast carrier transport characteristics and promoting the photo-generated electron-hole separation efficiency. The high specific surface areas, suitable and sizable band gaps, appropriate band edges, small effective carrier masses, and excellent optical absorption capability, all these exotic properties taken together, make penta carbides promising candidates for photocatalytic water splitting.

I. INTRODUCTION

The discovery of graphene, a one-atom-thick carbon layer of graphite, has given a significant boost to studies of two-dimensional (2D) nanomaterials owing to its outstanding properties such as high carrier mobility, superior thermal conductivity, outstanding optical transparency, and mechanical flexibility [1,2]. The lack of band gap, which is the major drawback to graphene, has greatly limited its potential applications in electronic and optoelectronic nanodevices. Targeting "beyond graphene," scientists have given attention to other inorganic 2D nanomaterials [3,4]. A great deal of effort has been made to the synthesis of graphenelike elemental group-IV materials, referred to as group-IV X-enes, including silicene [5,6], germanene [5,7,8], and stanane [9], which are semimetals and behave like a massless Dirac fermion as in graphene. Unlike planar graphene, the group-IV X-enes are naturally buckled. The buckled structure of group-IV X-enes leads to the band-gap opening by applying a vertical electric field [10]. Moreover, the buckled nature could be easily functionalized through chemical reactions, which also induces a band-gap opening [11]. Contrary to the group-IV X-enes, the group-IV binary carbides (SiC, GeC, and SnC) are planar honeycomb structures, have desirable band gaps [12] and exhibit remarkable catalytic activity for oxygen reduction reaction (ORR) and NO reduction [13–15].

Recently, a new carbon allotrope, penta graphene, composed of only pentagons, presents many novel properties going beyond graphene [16]. The synthesis of pentagonal Si nanoribbons in 2016 [17,18] inspires new efforts on the 2D pentagonal group-IV materials. Recently, intensive attempts have been devoted to the modeling of the Si, Ge, and Sn counterparts of penta graphene, namely penta silicene, penta germanene, and penta stanene, respectively [19–22]. Aierken *et al.* have demonstrated that the bilayer penta silicene is the most stable form of bilayer silicon predicted so far and exhibits interesting tunable properties [19]. The stable form of penta silicene and penta germanene presents the ultralow thermal conductivities (1.29 Wm^{-1} K^{-1} and 0.30 Wm^{-1} K^{-1}, respectively) [21]. Furthermore, penta stanene is energetically more favorable than the free-standing stanene synthesized on a Bi$_2$Te$_3$(111) substrate [9], however, exhibits poor stability due to the presence of imaginary phonon modes. In contrast, its hydrogenated and fluorinated derivatives are found to be dynamically stable and proposed as photocatalyst candidates for water splitting [22]. Accordingly, Li *et al.* declared that pentagonal silicon carbide (p-SiC$_2$) could exist in 2D stable form, and promising photocatalyst for water splitting [23]. However, our best knowledge, except for p-SiC$_2$, 2D pentagonal group-IV binary and ternary carbides are not reported yet.

Unlike individual C atoms, the C$_2$ dimers as an important unit in the growth of many carbon structures, play a

─────────
[*]mekilic@kist.re.kr
[†]krlee@kist.re.kr

special role in the stability of carbides [24–26]. For instance, Joswig *et al.* have studied the influence of C_2 dimers on the stability of Ti_mC_n clusters and found that the clusters containing C_2 dimers are energetically more stable as compared to those containing individual carbons [27]. The C_2 dimers in carbides improve not only the gain stability but also endow novel properties [28–30], playing an important role in promoting the experimental realization. Very recently, we have proposed 2D tetrahexagonal group-IV carbides containing C_2 dimers (*th-X*C_2 where X = Si, Ge, Sn), possessing robust stability, sizable direct band gap, and anisotropic high carrier mobility for nanoelectronics [31]. We showed that *th-*SiC$_2$ can be perfectly formed by applying the Stone-Wales (SW) transformation to *penta-*SiC$_2$. In addition to *penta-*SiC$_2$, the predicted *th-X*C_2 carbides can assure the existence of other 2D penta carbides. Inspired by the *th-X*C_2 and their appealing properties for nanoelectronics, we have designed a series of 2D pentagonal binary and ternary carbides, namely penta carbides, containing C_2 dimers using the state-of-the-art first-principle density functional theory (DFT) calculations. The thermodynamic, dynamic, thermal, and mechanical stabilities of penta carbides have been investigated by evaluating total energy calculations, phonon lattice dynamics calculations, *ab initio* molecular dynamics (AIMD) calculations, and elastic constant calculations, respectively. After verifying their great stabilities, we have systematically studied their structural, mechanical, electronic, and optical properties and finally revealed their potential applications for nanoelectronics and photocatalytic water splitting.

II. METHOD

The DFT calculations were performed using the Vienna Ab-initio Simulation Package (VASP) [32,33]. The core electrons were described by pseudopotentials constructed with the Projector Augmented Wave (PAW) [34]. The exchange and correlation energies were calculated with the functional of Perdew, Burke, and Ernzerhof (PBE) in the generalized gradient approximation (GGA) [35]. A plane wave with a cutoff energy of 520 eV was used. A vacuum region of 20 Å was added along the out-of-plane direction to ensure that no appreciable interaction occurs between two adjacent layers. The k points in reciprocal space were sampled using Γ-centered Monkhorst-Pack scheme [36] with $24 \times 24 \times 1$ grid. The atomic relaxation was carried out until the change in the total energy and atomic force components per unit cell was smaller than 10^{-5} eV and 10^{-4} eV Å^{-1}, respectively, where the maximal stress tensor component was less than 10 kbar. The Gaussian-type smearing method was set to be 0.01 eV and was increased to 0.05 eV for density-of-states calculations. The phonon calculations were carried out by finite displacement method with supercell approach ($5 \times 5 \times 1$ supercell for p-XC$_2$ and p^1-$X_{0.5}Y_{0.5}$C$_2$ and $4 \times 4 \times 1$ super cell for p^2-$X_{0.5}Y_{0.5}$C$_2$ nanosheets were used) where the convergence criterion of the total energy was set as 1×10^{-8} eV per unit cell using the PHONOPY package [37]. Moreover, the AIMD simulations were performed under the constant volume and temperature (NVT ensemble) where temperature T was controlled by employing the Nose-Hover thermostat [38–40]. The AIMD simulations run for a total simulation time of 6 ps with
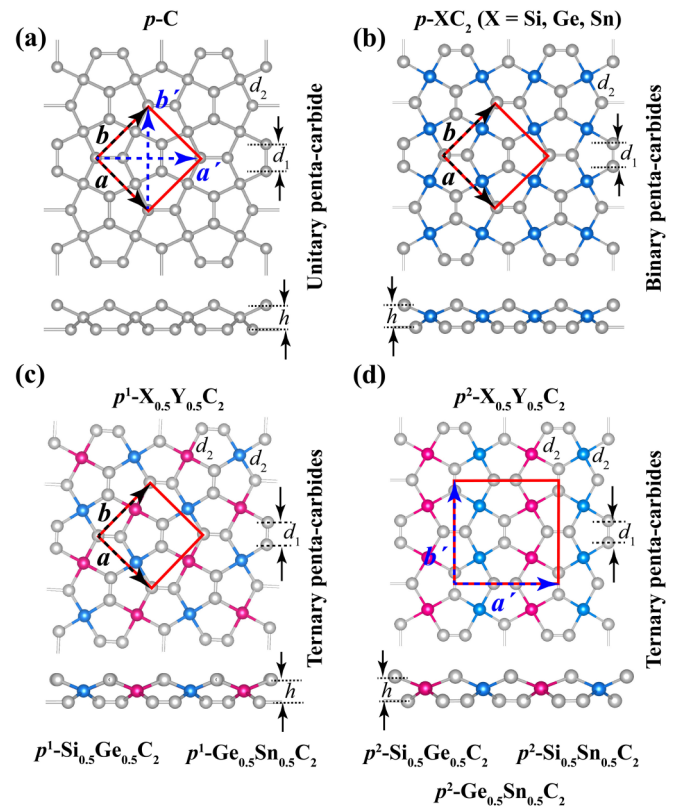

FIG. 1. Top and side views of the atomic structures of (a) the unitary (p-C), (b) binary (p-XC$_2$), and (c) and (d) ternary (p^1-$X_{0.5}Y_{0.5}$C$_2$ and p^2-$X_{0.5}Y_{0.5}$C$_2$) penta carbides. Gray and sky blue/pink balls represent carbon and X (or Y) atoms where X (or Y) is Si, Ge, and Sn, respectively. The unit cells are framed by red line in the inset.

time steps of 1 fs at 900 K using large supercells, which are the same as used in the phonon calculations. For the calculations of electronic properties, we employed the Heyd-Scuseria-Ernzerhof hybrid functional (HSE06), constructed by mixing 25% of the nonlocal Fock exchange with 75% of the PBE exchange, and 100% of the PBE correlation energy [41,42] as the PBE functional fails to capture correctly the electronic band-gap and band edge positions of penta carbides. Moreover, the optical response calculations were carried out using the quasiparticle many-body GW$_0$ approximation [43] with a cutoff energy of 480 eV. In order to achieve the numerical accuracy in the GW$_0$ virtual orbitals were chosen 3 times greater than the number of occupied bands. The optical absorption spectra including electron (e)-hole (h) interactions were calculated *via* the Bethe-Salpeter equation (BSE) [44].

III. Results and Discussions

A. Structure characterization

The atomic structures of the unitary, binary, and ternary pentagonal structures are presented in Fig. 1. The unitary penta carbide (p-C), or penta graphene, is composed of three-fold (sp^2) and fourfold (sp^3) coordinated carbons [Fig. 1(a)]. The binary penta carbides, formulated as p-XC$_2$ where X = Si, Ge, Sn, were constructed by alternately replacing the fourfold coordinated carbons with X atoms in p-C and keep-

TABLE I. Calculated structure parameters for the unitary (p-C), binary (p-XC$_2$), and ternary (p^1-$X_{0.5}Y_{0.5}$C$_2$ and p^2-$X_{0.5}Y_{0.5}$C$_2$) penta carbides. The lattice constants a (a') and b (b'), layer thickness h, bond lengths d_1 for C=C and d_2 for X–C (or Y–C) in Å, the cohesive energy E_{coh} in eV/atom, the electronic band-gap energy E_g^{PBE} (at the PBE functional level) and E_g^{HSE06} (at the HSE06 hybrid functional level) in eV, and band-gap type (direct or indirect) are presented for all the considered structures.[a]

	a (a') (Å)	b (b') (Å)	h (Å)	d_1 (Å)	d_2 (Å)	E_{coh} (eV/atom)	E_g^{PBE} (eV)	E_g^{HSE06} (eV)	Type
p-C	3.641[a]	3.641	1.205	1.339	1.550	6.77	2.38	3.26	Indirect
p-SiC$_2$	4.410	4.410	1.325	1.362	1.908	5.29	1.49	2.39	Indirect
p-GeC$_2$	4.602	4.602	1.373	1.344	2.008	4.69	1.60	2.23	Indirect
p-SnC$_2$	5.045	5.045	1.388	1.337	2.215	3.83	1.02	1.36	Indirect
p^1-Si$_{0.5}$Ge$_{0.5}$C$_2$	4.506	4.506	1.343	1.353	1.924[b1]–1.992[b2]	4.98	1.49	2.28	Indirect
p^1-Ge$_{0.5}$Sn$_{0.5}$C$_2$	4.825	4.825	1.386	1.342	2.069[b2]–2.158[b3]	4.22	1.27	1.78	Indirect
p^2-Si$_{0.5}$Ge$_{0.5}$C$_2$	6.376	6.366	1.355	1.352	1.909[b1]–2.006[b2]	4.99	1.24	2.14	Indirect
p^2-Si$_{0.5}$Sn$_{0.5}$C$_2$	6.709	6.627	1.373	1.353	1.917[b1]–2.202[b3]	4.50	0.63	1.35	Indirect
p^2-Ge$_{0.5}$Sn$_{0.5}$C$_2$	6.831	6.798	1.393	1.342	2.020[b2]–2.201[b3]	4.24	0.85	1.54	Indirect

[a]The b_1, b_2, and b_3 superscripts indicate the bond length of Si–C, Ge–C, and Sn–C for the ternary penta carbides, respectively.

ing the position of threefold coordinated carbons (C$_2$ dimers) [Fig. 1(b)]. The p-XC$_2$ nanosheets belong to the $P\overline{4}21m$ symmetry (no 113) where the unit cell consists of two X and four C atoms so that each X atom is fourfold coordinated and each C atom is threefold coordinated. For the ternary penta carbides, two different ternary alloys, namely p^1-$X_{0.5}Y_{0.5}$C$_2$ and p^2-$X_{0.5}Y_{0.5}$C$_2$, were studied in the present work. By replacing one X atom with another group-IV element (Y) in the unit cell of p-XC$_2$, we constructed p^1-$X_{0.5}Y_{0.5}$C$_2$ [X (or Y) = Si, Ge, Sn] nanosheets [Fig. 1(c)]. The p^1-$X_{0.5}Y_{0.5}$C$_2$ ternary alloys posses the $P\overline{4}$ symmetry (no 81) where the unit cell is composed of six atoms with X:Y:C ratio of 1:1:4. By varying the size of the cell from the unit cell to supercell, we built p^2-$X_{0.5}Y_{0.5}$C$_2$ [X (or Y) = Si, Ge, Sn] ternary alloys [Fig. 1(d)]. The p^2-$X_{0.5}Y_{0.5}$C$_2$ nanosheets belong to the $Pma2$ symmetry (no 28) where the unit cell includes twelve atoms with X:Y:C ratio of 2:2:8.

The lattice constants a (a') and b (b') were determined for p-C, p-XC$_2$, and p^1-$X_{0.5}Y_{0.5}$C$_2$ (p^2-$X_{0.5}Y_{0.5}$C$_2$) as depicted in Fig. 1. For p-C, p-XC$_2$, and p^1-$X_{0.5}Y_{0.5}$C$_2$, the **a** and **b** lattice directions are symmetric and the structures are invariant under 90° rotation of the coordinate axis. For p^2-$X_{0.5}Y_{0.5}$C$_2$, however, the **a$'$** and **b$'$** lattice directions are not symmetric and the structure is not invariant under the symmetry transformation. The lattice vectors $\vec{a}'$ and $\vec{b}'$ of p^2-$X_{0.5}Y_{0.5}$C$_2$ can be defined as $\vec{a}' = \vec{a} + \vec{b}$ and $\vec{b}' = \vec{a} - \vec{b}$ where $\vec{a}$ and $\vec{b}$ are the lattice vectors of p-XC$_2$ and p^1-$X_{0.5}Y_{0.5}$C$_2$. Also, one can easily see that the C=C bonds in p-XC$_2$ and p^1-$X_{0.5}Y_{0.5}$C$_2$ lie in the diagonal lattice direction (**ab**), whereas the C$_2$ dimers in p^2-$X_{0.5}Y_{0.5}$C$_2$ lie in the **a$'$** and **b$'$** lattice directions. The corresponding lattice constants, layer thickness h, C$_2$ dimer bond length d_1, and X (or Y)–C bond length d_2 of penta carbides were summarized in Table I.

To benchmark our calculations, we first analyzed penta graphene. The optimized lattice constant of p-C is about $a = b = 3.641$ Å with the layer thickness of $h = 1.205$ Å. The calculated C=C bond length is $d_1 = 1.339$ Å. The bond length between three- and fourfold coordinated adjacent carbon atoms is found to be $d_2 = 1.550$ Å. All these obtained values are in agreement well with Zhang $et\ al.$ [16]. For p-SiC$_2$

monolayer, the optimized lattice constant is $a = b = 4.410$ Å. The elongation of lattice constant is caused by the larger size of Si atom as compared to C. The carbon dimer bond length in p-SiC$_2$ is calculated as $d_1 = 1.362$ Å, which is 0.02 Å smaller than that in p-C, indicating pronounced character of carbon double bonds. From p-C to p-SiC$_2$, the presence of Si does not affect the bond behavior of C$_2$ dimer whereas it increases the d_2 bond length by 0.36 Å and the layer thickness by 0.12 Å. Thus, the substitution of 4-fold coordinated C atom by Si atom in penta graphene induces the elongation of d_2, h, and thereby the lattice constants. The calculated Si–C bond length in p-SiC$_2$ as $d_2 = 1.908$ Å is in the range of the standard Si–C bond length as 1.903 Å in th-SiC$_2$ [31], 1.87–1.92 Å in t-SiC [45], 1.916 Å in $sila$-SiC$_2$ [46], 1.883 Å in th-SiC [47]. The obtained results for p-SiC$_2$ agree well the previous report [48]. For p-GeC$_2$, the calculated lattice constant ($a = b = 4.602$ Å) is greater than that of p-C and p-SiC$_2$. The reason is that the atom size of Ge is about 4% larger than Si, resulting in the increase of d_2 and h. The Ge–C bond length is calculated as $d_2 = 2.008$ Å, which is comparable with that of t-GeC (2.063 Å), c-GeC (2.006 Å) [47], and th-GeC$_2$ (2.014 Å) [31]. The C=C bond length remain almost constant ($d_1 = 1.344$ Å) as we expect. Likewise, the lattice constant of p-SnC$_2$ is critically increased as $a = b = 5.045$ Å due to the larger size of Sn with respect to Ge. The calculated Sn–C bond length (about 2.215 Å) is slightly larger than the standard Sn–C bond length (about 2.14–2.18 Å) [49]. In general, the lattice constants, X–C bond length, and layer thickness of p-XC$_2$ are elongated with increasing the atomic number of X (X = Si, Ge, Sn), whereas the C=C bond length is not affected by the presence of X atom (slightly changed by varying X atom). For the ternary penta carbides, the corresponding lattice parameters are found to be in between their binary counterparts. For instance, the corresponding lattice parameters of p^1-Si$_{0.5}$Ge$_{0.5}$C$_2$ are in between those of p-SiC$_2$ and p-GeC$_2$. Remarkably, ternary alloying enables the direct modification of atomic bonding, and thereby structural, mechanical, and electronic properties properties of penta carbides.
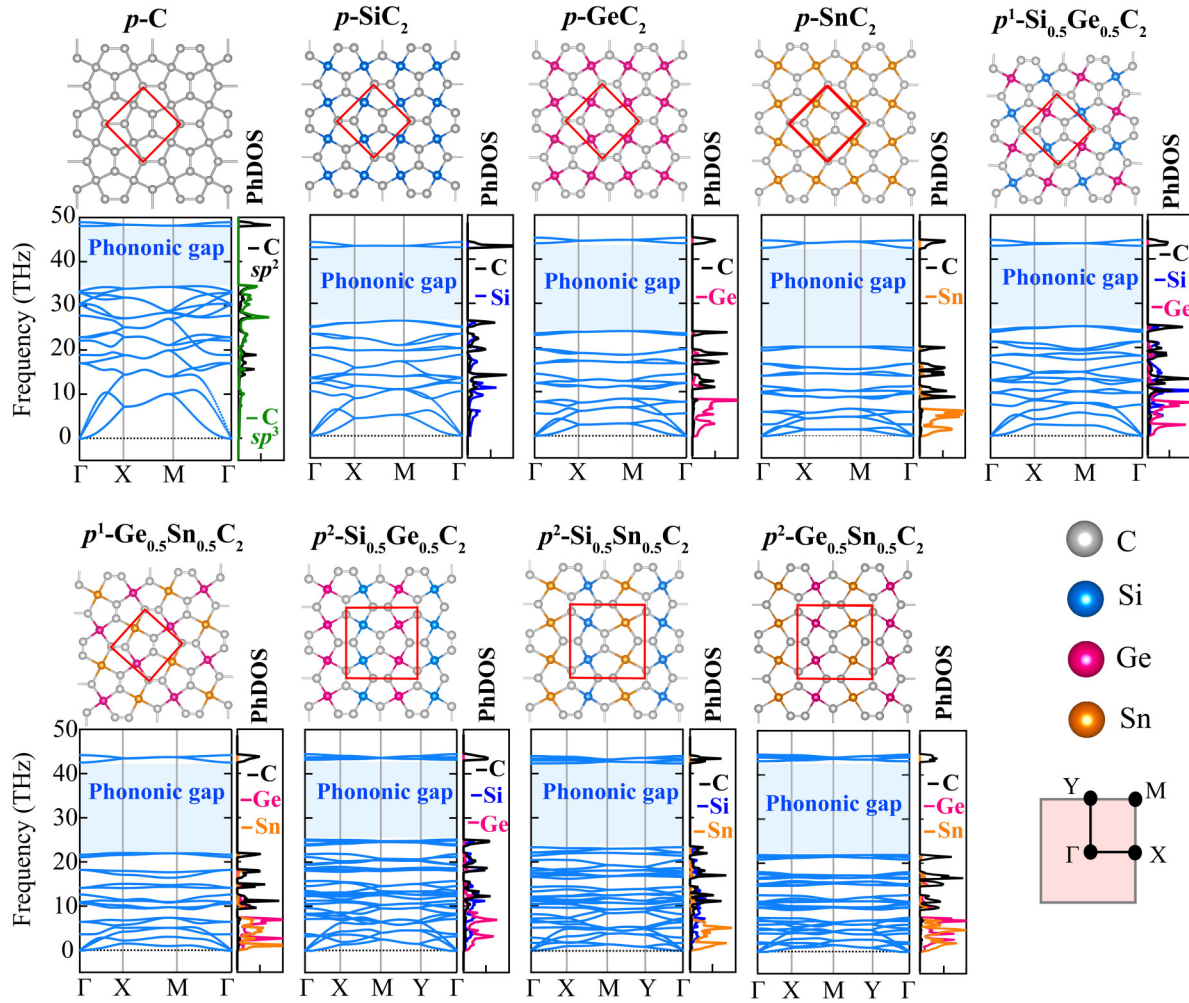
FIG. 2. Phonon dispersion curves along the path passing through the high-symmetry k-points in the irreducible Brillouin zone (BZ) and atom-projected density-of-states (PhDOS) of the unitary (p-C), binary (p-XC$_2$), and ternary (p^1-$X_{0.5}Y_{0.5}$C$_2$ and p^2-$X_{0.5}Y_{0.5}$C$_2$) penta carbides.

B. Structure stability

1. Energetic stability

To examine the energetic stability of penta carbides, we computed the cohesive energy defined as $E_{coh} = (nE_C + mE_X - E_{PC})/(n + m)$ where E_{PC} is the total energy of penta carbide, E_C and E_X denote the energy of the isolated C and X ($X = $ Si, Ge, Sn) atoms, respectively. Moreover, n and m are the number of C and X atoms in the unit cell, respectively. According to this definition, a more positive E_{coh} value indicates a more thermodynamically (or energetically) stable structure. We calculated the cohesive energy of penta graphene as 6.77 eV per atom, which is close to the previous value of 6.84 eV per atom [50]. For the binary penta carbides, the cohesive energy of p-SiC$_2$, p-GeC$_2$, and p-SnC$_2$ is found to be 5.29 eV per atom, 4.69 eV per atom, and 3.83 eV per atom, respectively, which are the lower than that of graphene (7.95 eV/atom), but higher than that of silicene (3.71 eV per atom) [51], and phosphorene (3.61 eV per atom) [52]. For the ternary penta carbides, the cohesive energy ranges from 4.22 to 4.99 eV per atom, listed in Table I. Thus, the calculated cohesive energy of penta carbides is clear evidence that they are a strongly bonded network.

2. Dynamics stability and phonon gap engineering by alloying and hydrogenation

To further test the dynamic stability of penta carbides, we performed the lattice dynamics phonon calculations. The phonon band dispersions were plotted in Fig. 2. Our first-principles calculations yield that no appreciable imaginary phonon modes in the whole BZ are available, indicating that the predicted penta carbides are dynamically stable. According to the lattice dynamics calculations, we also noted that p^1-Si$_{0.5}$Sn$_{0.5}$C$_2$ ternary alloy is dynamically unstable with an imaginary phonon mode (see Fig. S1 of the supplemental material [53]). Remarkably, the highest phonon frequency of p-C, p-SiC$_2$, p-GeC$_2$, and p-SnC$_2$ is calculated as 1632, 1464, 1497, and 1476 cm^{-1}, respectively. Such high frequency values in the phonon dispersions of penta carbides mean that they own robust $X-$C ($X = $ Si, Ge, Sn) and C=C bonds.

The phonon band gap in the material provides the ability to prohibit the propagation of mechanical waves in certain frequency ranges. Remarkably, penta carbides have the phonon band gap between ~800 cm^{-1} and ~1500 cm^{-1} in the phonon dispersion curves. The phonon gap makes penta carbides useful materials for phononic device applications such as phonon waveguides, cavities,

TABLE II. Calculated elastic constants C_{ij} in N/m, Young's modulus $Y_{a(a')}$ and $Y_{b(b')}$ in N/m, Poisson's ratio $\nu_{ab(a'b')}$ and $\nu_{ba(b'a')}$, and ultimate tensile strain $UTS_{a(a')}$, $UTS_{b(b')}$, and $UTS_{ab(ab')}$ of the unitary (p-C), binary (p-XC_2), and ternary (p^1-$X_{0.5}Y_{0.5}C_2$ and p^2-$X_{0.5}Y_{0.5}C_2$) penta carbides.

	C_{11}	C_{22}	C_{12}	C_{66}	$Y_{a(a')}$	$Y_{b(b')}$	$\nu_{ab(a'b')}$	$\nu_{ba(b'a')}$	$UTS_{a(a')}$	$UTS_{b(b')}$	$UTS_{ab(ab')}$
p-C	267.54	267.54	-18.81	150.95	266.22	266.22	-0.070	-0.070	17	17	21
p-SiC$_2$	138.71	138.71	4.82	73.01	138.54	138.54	0.035	0.035	21	21	16
p-GeC$_2$	122.24	122.24	8.48	63.60	121.65	121.65	0.069	0.069	16	16	12
p-SnC$_2$	83.83	83.83	14.76	44.49	81.23	81.23	0.176	0.176	9	9	7
p^1-Si$_{0.5}$Ge$_{0.5}$C$_2$	131.65	131.65	6.53	68.14	131.33	131.33	0.050	0.050	18	18	14
p^1-Ge$_{0.5}$Sn$_{0.5}$C$_2$	97.26	97.26	13.12	51.89	95.49	95.49	0.135	0.135	12	12	10
p^2-Si$_{0.5}$Ge$_{0.5}$C$_2$	136.84	137.32	1.06	62.24	136.83	137.32	0.008	0.008	15	21	13
p^2-Si$_{0.5}$Sn$_{0.5}$C$_2$	116.78	112.31	4.57	45.83	116.60	112.13	0.039	0.041	15	19	10
p^2-Ge$_{0.5}$Sn$_{0.5}$C$_2$	109.22	105.70	4.15	44.20	109.06	105.54	0.038	0.039	10	14	9

filters, etc. From the unitary to binary penta carbides, we observed that the position and width of the phonon gap are considerably affected by the presence of X ($X =$ Si, Ge, Sn) atoms. More specifically, from p-C to p-SiC$_2$, the upper and lower frequencies of the phonon gap in the phonon dispersion curves shift to lower value. It is worth to note that the phonon gap in penta graphene can be adjusted by substituting fourfold coordinated carbon atoms with Si, Ge, or Sn atoms. Surprisingly, for binary and ternary penta carbides, the upper frequency of the phonon gap remains almost unchanged. To understand the contribution of atoms to the phonon vibration spectrum in penta carbides, we plotted the atom-projected phonon density-of-states (PhDOS) in Fig. 2. The PhDOS results revealed that the high-frequency phonon modes are mainly characterized by the motion of the threefold coordinated carbons (C$_2$ dimers) while the main contribution to the low-frequency modes is dominated by fourfold coordinated atoms. Thus, the upper frequency of the phonon gap is not affected by the atomic mass difference between the constituents. On the other hand, the lower frequency of the phonon gap gradually shifts to lower frequency with increasing atomic number of X ($X =$ Si, Ge, and Sn) going from Si to Sn due to the increasing the atomic

mass difference between C and X atoms. We noted that the increase of the atomic mass difference results in the weaker $X-$C bond strength and causes much less dispersive phonon branches. For the ternary penta carbides, the lower frequency of the phonon gap in the phonon dispersion curves varies by changing the constituent elements. Thus, the phonon gap in penta carbides can be modulated by alloy engineering.

In our previous study, we have reported that the phonon gap in tetrahexcarbon (constructed from penta graphene by applying the SW transformation) can be tuned by hydrogenation and fluorinations [54,55]. Likewise, we studied the full hydrogenation of p-SiC$_2$, namely p-SiC$_2$H$_2$. The lattice dynamics results revealed that all the phonon modes are free from imaginary frequencies throughout the BZ, indicating the dynamical stability of p-SiC$_2$H$_2$ (Fig. S2 of the supplemental material [53]). On the hydrogenation of p-SiC$_2$, the highest optical phonon branches around 1500 cm^{-1} characterized by the vibration frequency of C$_2$ dimers disappeared as the sp^2-hybridized carbons are changed to sp^3-hybridized ones. Therefore, the size and width of the phonon gap at which the vibration frequencies are forbidden to propagate in penta carbides can be modulated by hydrogenation and alloy engineering.
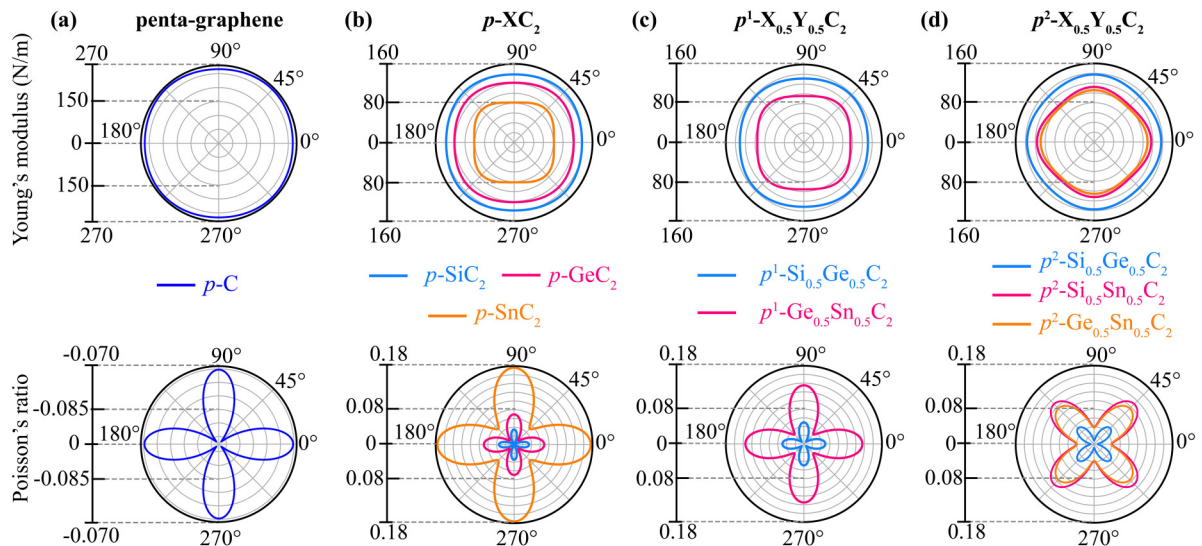

FIG. 3. Angle-dependent Young's modulus $Y(\theta)$ (upper panel) and Poisson's ratio $\nu(\theta)$ (lower panel) of the unitary (p-C), binary (p-XC_2), and ternary (p^1-$X_{0.5}Y_{0.5}C_2$ and p^2-$X_{0.5}Y_{0.5}C_2$) penta carbides.
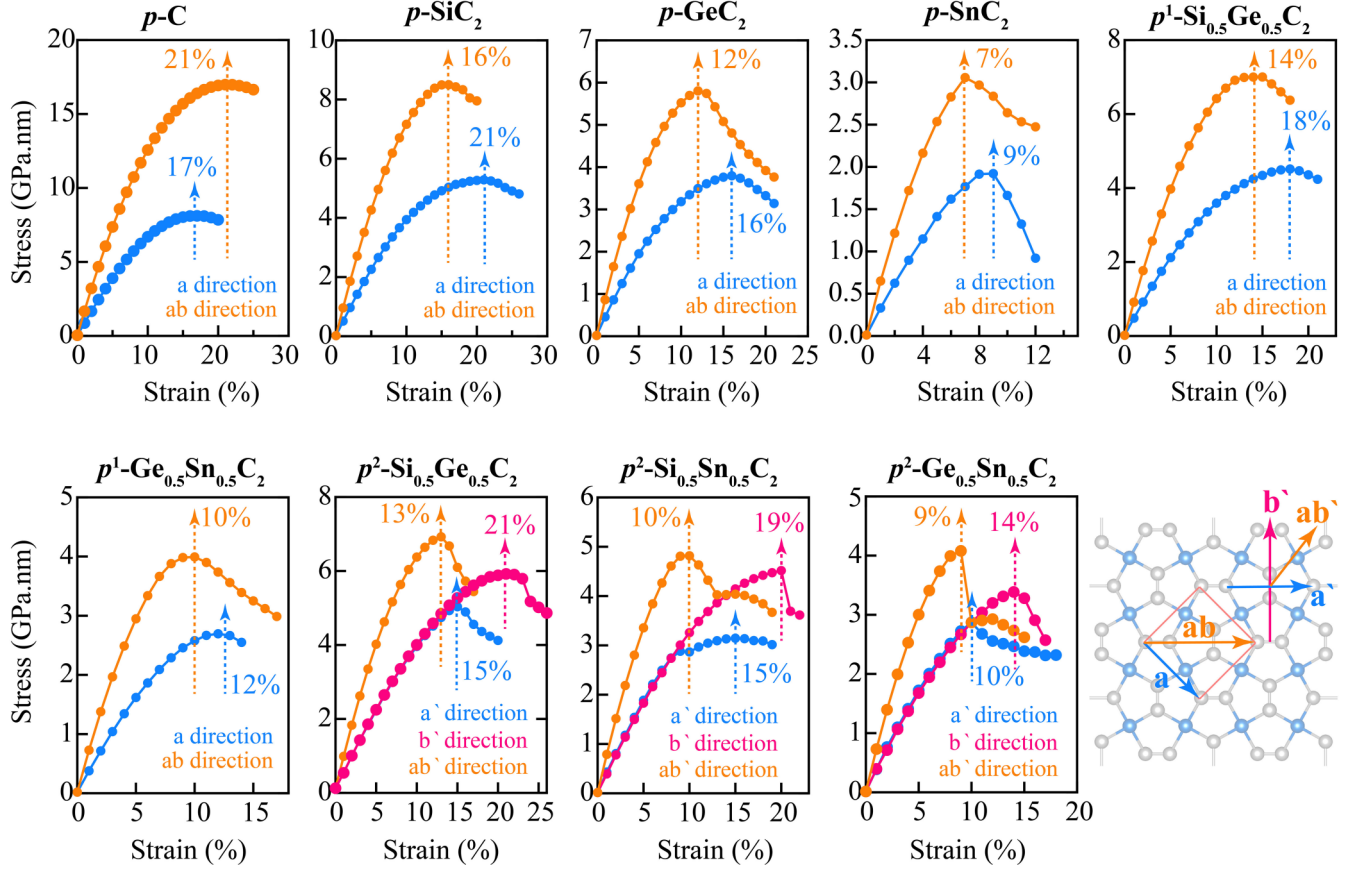
FIG. 4. Stress-strain relationship for uniaxial strain along the **a(a′)** direction and biaxial strain along the **ab(ab′)** directions for p-C, p-XC$_2$, and p^1-$X_{0.5}Y_{0.5}$C$_2$ (p^2-$X_{0.5}Y_{0.5}$C$_2$) where X or Y = Si, Ge, Sn.

3. Thermal stability

The thermal stability of penta carbides was evaluated by employing the AIMD simulations using canonical ensemble at 800 K (except for p-SnC$_2$ performed at 600 K) for 6 ps. A 5×5 supercell for p-C, p-XC$_2$, and p^1-$X_{0.5}Y_{0.5}$C$_2$ and 4×4 supercell for p^2-$X_{0.5}Y_{0.5}$C$_2$ were used to reduce the artificial physical lattice constraints due to the use of periodic boundary conditions. As the energy of 2D materials is sensitive to the bond lengths and bond angles, we plotted the variation of total energy of penta carbides with respect to the simulation time, enabling us to monitor the possible bond breaking or bond reforming. Obviously, the total energy of penta carbide nanosheets is stabilized around 1 ps (Fig. S3 of the supplemental material [53]). Moreover, no structural reformations in the atomic configurations of penta carbides is observed at the end of the AIMD simulation (6 ps). Thus, the AIMD results indicated that the predicted penta carbides have good thermal stability, and maintain their structural integrities under thermal shock.

4. Mechanical stability

To ensure whether penta carbides have enough in-plane stiffness, we calculated their elastic constants. More generally, the elastic constants play an important role in providing fundamental information on the mechanical stability, stiffness, brittleness, ductility, etc. The mechanical stability of penta carbides was evaluated by the elastic stability criteria [56] as $C_{11}C_{22} - C_{12}^2 > 0$ and $C_{66} > 0$ where C_{ij} are the in-plane elastic stiffness constants. The corresponding elastic constants were obtained by computing the stress generated by applying a small strain within the harmonic approximation. The energy change per unit area $U_s(\varepsilon)$, associated with the small distortions in penta carbides is calculated as

$$U_s(\varepsilon) = \tfrac{1}{2}C_{11}\varepsilon_x^2 + \tfrac{1}{2}C_{22}\varepsilon_y^2 + C_{12}\varepsilon_x\varepsilon_y + 2C_{66}\varepsilon_{xy}^2, \quad (1)$$

$$\text{uniaxial-x strain} \rightarrow (\varepsilon_y, \varepsilon_{xy} = 0), \, U_s(\varepsilon) = \tfrac{1}{2}C_{11}\varepsilon_x^2, \quad (2)$$

$$\text{uniaxial-y strain} \rightarrow (\varepsilon_x, \varepsilon_{xy} = 0), \, U_s(\varepsilon) = \tfrac{1}{2}C_{22}\varepsilon_y^2, \quad (3)$$

$$\text{biaxial} \rightarrow (\varepsilon_x = \varepsilon_y), (\varepsilon_{xy} = 0), U_s(\varepsilon)$$
$$= \left(\tfrac{1}{2}C_{11} + \tfrac{1}{2}C_{22} + C_{12}\right)\varepsilon_x^2, \quad (4)$$

$$\text{shear strain} \rightarrow (\varepsilon_x, \varepsilon_y = 0), \, U_s(\varepsilon) = 2C_{66}\varepsilon_{xy}^2, \quad (5)$$

where ε_{ij} is the corresponding infinitesimal strain defined as $\varepsilon_i = (L_i' - L_i)/L_i$ ($i = x, y$) where L_i' and L_i are the strained and unstrained lattice parameters (Voigt notations were adopted here as, $1 \equiv xx$; $2 \equiv yy$; $6 \equiv xy$). We plotted the variation of strain energy with respect to in-plane uniaxial, biaxial, and various shear strains in Fig. S4 of the
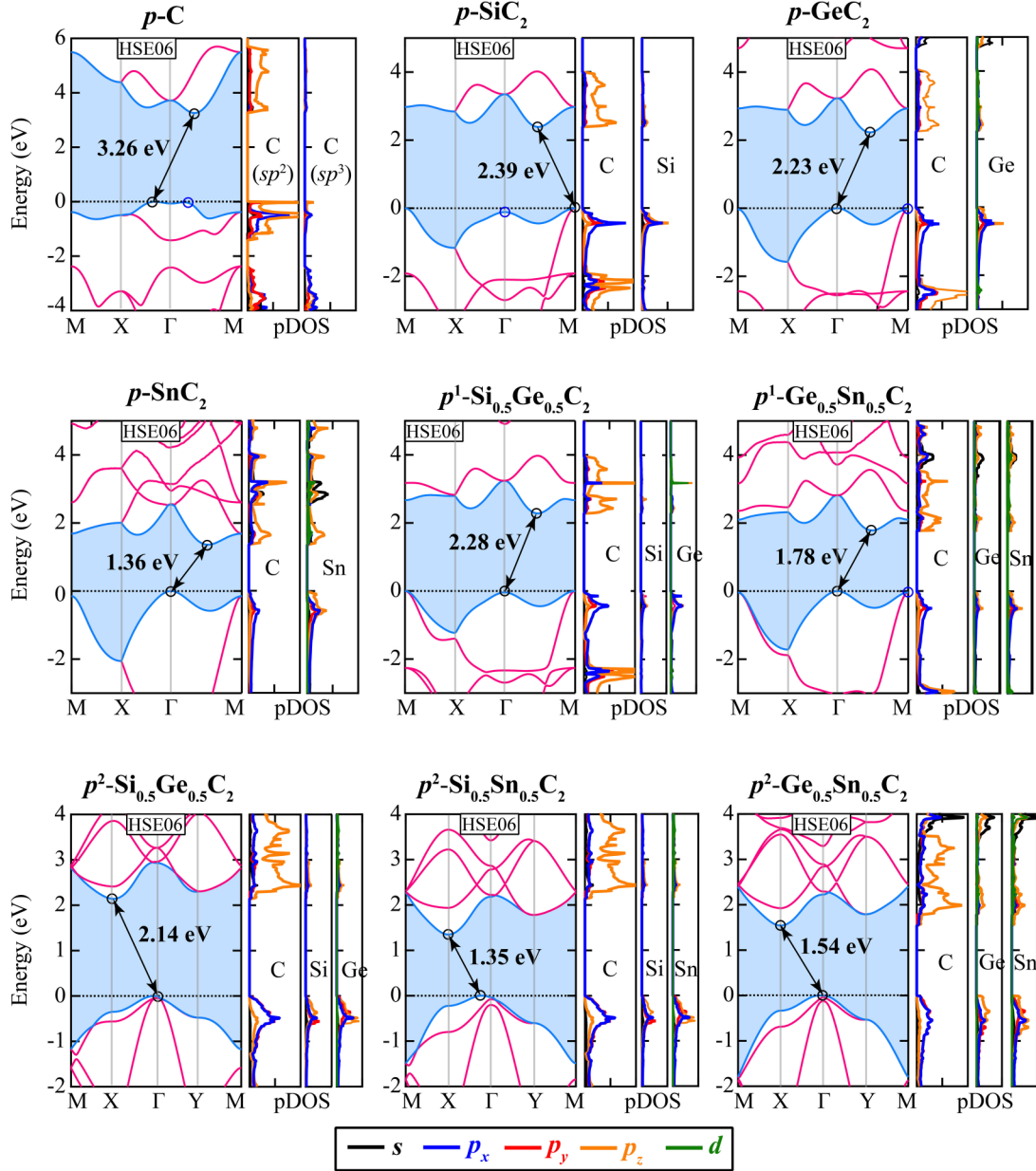
FIG. 5. Calculated electronic band structures and atom- and orbital-projected density of states (pDOS) (at the HSE06 level) for the unitary (p-C), binary (p-XC$_2$), and ternary (p^1-$X_{0.5}Y_{0.5}$C$_2$ and p^2-$X_{0.5}Y_{0.5}$C$_2$) penta carbides. In the electronic band structures, the VBM and CBM bands are depicted by sky blue lines, and the Fermi energy indicated by black dashed line is set to 0 eV. In the pDOS, the s, p_x, p_y, p_z, and d orbitals are denoted by black, blue, red, orange, and green, respectively.

supplemental material [53]. The applied strain ε_i varies from -0.020 to 0.020 in steps of 0.005 for each type of lattice deformations in the present calculations. The obtained elastic constants summarized in Table II obey the elastic stability criteria, accordingly, confirming the mechanical stability of penta carbides.

C. Mechanical properties

After confirming the energetic, dynamical, thermal, and mechanical stability of penta carbides, we investigated their inherent mechanical properties, including anisotropic mechanical response, Young's modulus, Poisson's ratio, and ultimate strength. Based on the obtained elastic stiffness constants, we calculated angular-dependent Young's modulus $Y(\theta)$ and Poisson's ratio $\nu(\theta)$ of penta carbides using the following equations [57]:

$$Y(\theta) = \frac{C_{11}C_{22} - C_{12}^2}{C_{11}s^4 + C_{22}c^4 + \left[\frac{\left(C_{11}C_{22} - C_{12}^2\right)}{C_{66}} - 2C_{12}\right]s^2c^2} \quad (6)$$

$$\nu(\theta) = \frac{C_{12}(s^4 + c^4) - \left[C_{11} + C_{22} - \frac{\left(C_{11}C_{22} - C_{12}^2\right)}{C_{66}}\right]s^2c^2}{C_{11}s^4 + C_{22}c^4 + \left[\frac{\left(C_{11}C_{22} - C_{12}^2\right)}{C_{66}} - 2C_{12}\right]s^2c^2}, \quad (7)$$

where $s = \sin(\theta)$ and $c = \cos(\theta)$. As shown in Fig. 3, Young's modulus of penta carbides exhibits nearly isotropic behavior. As a benchmark to compare, we calculated Young's modulus of p-C as 267.54 N/m, agreeing well with the previous report ($Y = 263.8$ N/m) [16]. For the binary penta carbides, the calculated Young's modulus of p-SiC$_2$ (138.54 N/m) is higher than that of th-SiC$_2$ (79.55-85.06 N/m) [31] and lower than that of h-SiC (162.7 N/m) [58] and th-SiC (143.59 N/m) [47]. The Young's modulus of p-GeC$_2$ (121.65 N/m) is comparable with that of th-GeC$_2$ (123.76-110.43 N/m) [31] and th-GeC (118.83) [47] and smaller than that of h-GeC (143.8 N/m) [59]. The Young's modulus of p-SnC$_2$ is calculated as 81.23 N/m, which is lower than that of h-SnC about 123.02 N/m [60]. More generally, the value of Young's modulus decreases with increasing the atomic radii of X element in p-XC$_2$. For ternary penta carbides, we found that Young's modulus of ternary alloys is in between that of their corresponding binary counterparts. For instance, Young's modulus of p^1-Si$_{0.5}$Ge$_{0.5}$C$_2$ (about 131.65 N/m) is in between that of p-SiC$_2$ (about 138.71 N/m) and p-GeC$_2$ (about 122.24 N/m). The similar behavior is also observed for p^2-$X_{0.5}Y_{0.5}$C$_2$ ternary penta carbides. This suggests that continuously varying mechanical properties of penta carbides can be achieved by ternary alloying.

Next, we calculated the Poisson's ratio (PR) of penta carbides. The PR is defined as the ratio of transverse strain ($\varepsilon_{\text{trans}}$) to applied axial strain ($\varepsilon_{\text{axial}}$) ($\nu = -\frac{\varepsilon_{\text{trans}}}{\varepsilon_{\text{axial}}}$). When the axial strain is applied to p-C, p-XC$_2$, and p^1-$X_{0.5}Y_{0.5}$C$_2$ (p^2-$X_{0.5}Y_{0.5}$C$_2$) in the **a**(**a$'$**) direction, the transverse strain in the **b**(**b$'$**) direction is computed where the PR is expressed as $\nu_{\text{ab}(a'b')} = -\varepsilon_{\text{b}(b')}/\varepsilon_{\text{a}(a')}$. The obtained PR values of penta carbides are listed in Table II. Unlike penta graphene, the binary and ternary penta carbides display nonauxetic behavior with the near-zero and positive PR values. Notably, the Young's modulus of penta carbides shows relatively isotropic mechanical response whereas their PR is highly orientation-dependent (anisotropic) as shown in Fig. 3. The calculated PR of p-C (about -0.070) is in good agreement with the report of Zhang and coworkers (about -0.068) [16]. For the binary penta carbides, the PR increases with increasing the atomic number of X elements. For p-SiC$_2$, the PR varies spatially with a maximum value of 0.035 along the **a** and **b** directions and with a minimum value of 0.001 along the diagonal direction (**ab**). Likewise, for p-GeC$_2$, the maximal value of the PR (about 0.069) emerges in the **a** and **b** directions whereas the minimum value of the PR (about 0.011) lies in the diagonal direction. For p-SnC$_2$, the PR is found to be a relatively high value (about 0.176 along the **a** (or **b**) direction, and 0.051 along the diagonal direction). The similar behavior is observed in p^1-$X_{0.5}Y_{0.5}$C$_2$ ternary penta carbides. However, due to the lattice vector orientation, p^2-$X_{0.5}Y_{0.5}$C$_2$ penta carbides exhibit the near-zero PR value along the **a$'$** and **b$'$** direction and the maximum value emerges in the diagonal direction (**ab$'$**).

We further examine the ultimate tensile strength, which is another important mechanical property indicating the ability to withstand large tensile strains without failure. By applying uniaxial and biaxial strains (up to ~20–25% in steps of 1%) to penta carbides, we calculated the stress and plotted the
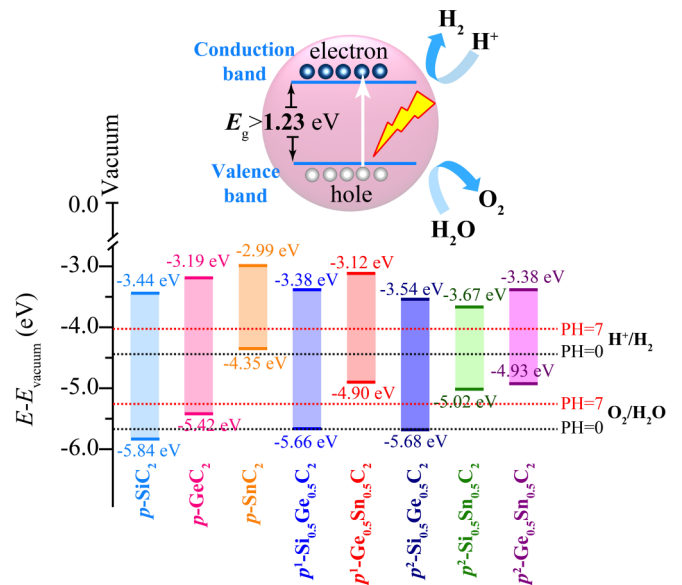

FIG. 6. Upper panel, schematic of band alignment for the migration of photo-generated electrons and holes. Lower panel, band edge alignment of the binary (p-XC$_2$) and ternary (p^1-$X_{0.5}Y_{0.5}$C$_2$ and p^2-$X_{0.5}Y_{0.5}$C$_2$) penta carbides with respect to the water reduction (H$^+$/H$_2$) and oxidation (O$_2$/H$_2$O) potentials at pH = 0 and pH = 7. The vacuum level is set to be zero.

stress-strain curves. The variation of stress with respect to the uniaxial and biaxial tensile strains is presented in Fig. 4. It can be readily seen that, within the small strain region (up to ~10%), the stress is almost linear dependent on the strain. For further strains, the stress continues to increase and reaches the maximum stress at a breaking point where the corresponding strain is termed the ultimate tensile strain (UTS). The UTS value of penta carbides is given in Table II. The stress-strain relationships imply that p-C can withstand tensile strains up to 17% for the uniaxial strain along the **a** direction and 21% for the equibiaxial strain (**ab** direction). The obtained UTS results for p-C agree well with the previous report [16]. For the binary penta carbides, the UTS of p-SiC$_2$ is found to be 21% for uniaxial strain along the **a** direction and and 16% for biaxial (**ab** direction) strain, respectively. We noted that p-SiC$_2$ can withstand a higher UTS value than p-C for uniaxial strain along the **a** direction. More generally, the UTS of the binary penta carbides follows the order of atomic number (or atomic radii) as p-SiC$_2 > p$-GeC$_2 > p$-SnC$_2$. For the ternary penta carbides, we found that the corresponding UTS values of p^1-Si$_{0.5}$Ge$_{0.5}$C$_2$ are in between those of p-SiC$_2$ and p-GeC$_2$. For p^2-$X_{0.5}Y_{0.5}$C$_2$ ternary penta carbides, the maximum UTS value emerges for uniaxial strain along the **b$'$** directions where the X (or Y) atoms uniformly distributed within these alloys. For instance, the UTS of p^2-Si$_{0.5}$Ge$_{0.5}$C$_2$ is calculated as 15%, 21%, and 13% for uniaxial strain along the **a$'$** and **b$'$** directions, and biaxial strain along the **ab$'$** direction, respectively.

D. Electronic properties

To further examine the electronic properties of penta carbides, we analyzed the electronic band structure, atom- and orbital-projected density of states (pDOS), and partial charge
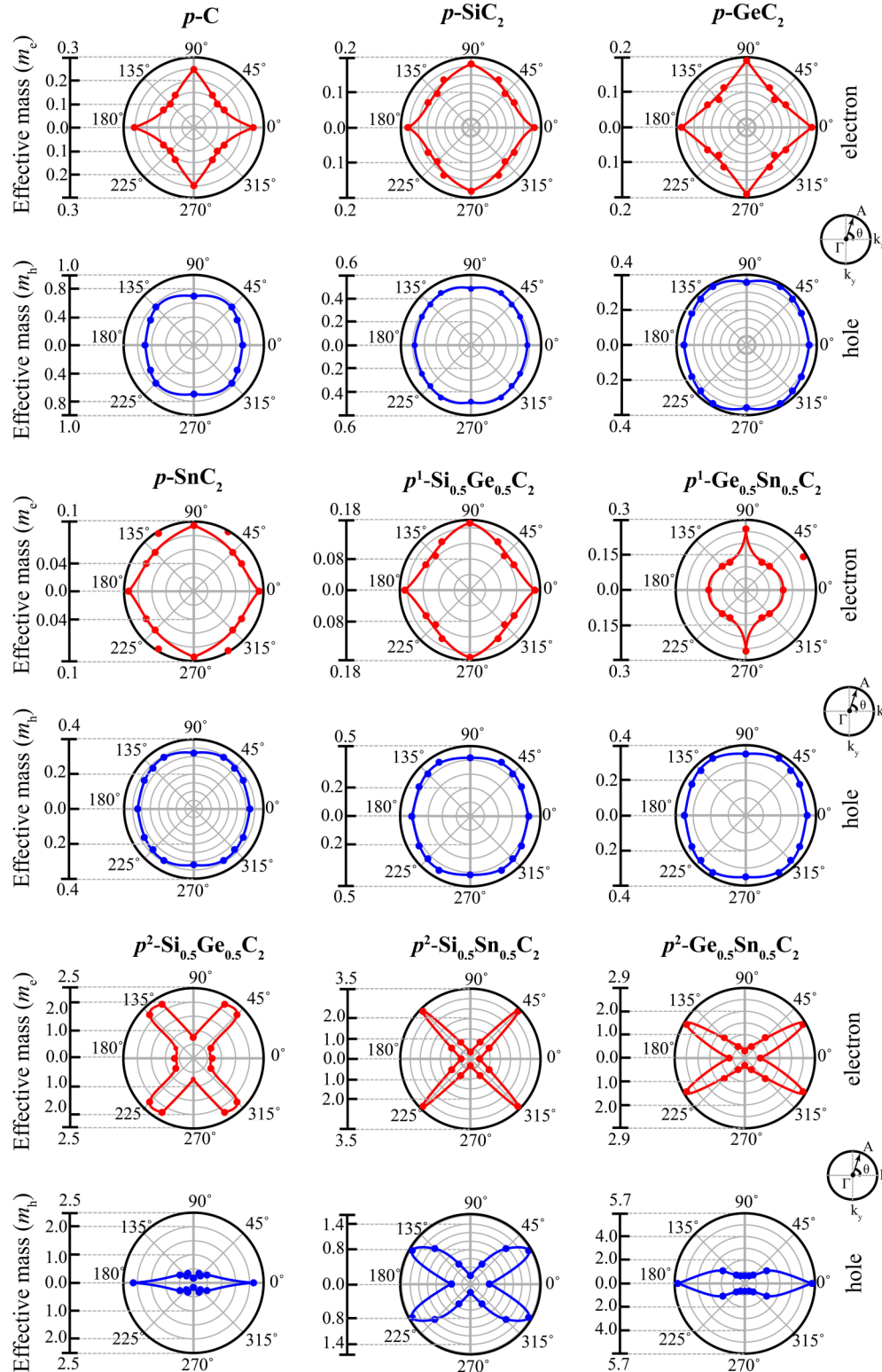
FIG. 7. Angular dispersion of electron effective mass (m_e) and hole effective mass (m_h) (computed by the HSE06 hybrid functional) for the unitary (p-C), binary (p-XC$_2$), and ternary (p^1-$X_{0.5}Y_{0.5}$C$_2$ and p^2-$X_{0.5}Y_{0.5}$C$_2$) penta carbides. Unit of effective mass is in mass of a free electron (m_0). k-vector along from Γ-X direction to Γ-A an arbitrary direction with angle of θ in inset is used.

density. Figure 5 shows the electronic band structure and pDOS of penta carbides at the HSE06 functional level. The band-gap energies were also calculated by the standard DFT method with PBE functional to the contrast. The band gaps

obtained by PBE and HSE06 methods are listed in Table I. The calculated electronic band structures revealed that penta carbides are semiconductors with desirable band-gap energies for nano- and optoelectronics. The obtained band gap of p-C

TABLE III. Effective mass of electron and hole in the unit of the free electron mass (calculated by the HSE06 method) along from Γ-X to Γ-A arbitrary directions.

Penta-carbides	Carriers	Effective mass (m_0)				
		Γ-X (0°)	Γ-A (30°)	Γ-A (45°)	Γ-A (60°)	Γ-Y (90°)
p-C	Electron	0.25	0.15	0.14	0.16	0.25
	Hole	0.70	0.71	0.77	0.90	0.70
p-SiC$_2$	Electron	0.18	0.14	0.14	0.16	0.18
	Hole	0.48	0.48	0.49	0.51	0.48
p-GeC$_2$	Electron	0.19	0.13	0.11	0.13	0.19
	Hole	0.36	0.36	0.37	0.38	0.36
p-SnC$_2$	Electron	0.09	0.08	0.08	0.10	0.09
	Hole	0.32	0.33	0.33	0.34	0.32
p^1-Si$_{0.5}$Ge$_{0.5}$C$_2$	Electron	0.17	0.13	0.12	0.14	0.17
	Hole	0.42	0.42	0.43	0.44	0.42
p^1-Ge$_{0.5}$Sn$_{0.5}$C$_2$	Electron	0.16	0.28	0.14	0.14	0.26
	Hole	0.35	0.35	0.36	0.38	0.35
p^2-Si$_{0.5}$Ge$_{0.5}$C$_2$	Electron	0.67	0.72	2.20	2.22	0.74
	Hole	2.14	0.56	0.35	0.39	0.17
p^2-Si$_{0.5}$Sn$_{0.5}$C$_2$	Electron	0.46	1.08	3.35	0.96	0.34
	Hole	0.44	1.56	1.17	0.54	0.20
p^2-Ge$_{0.5}$Sn$_{0.5}$C$_2$	electron	0.66	2.87	1.24	0.57	0.30
	hole	5.73	2.16	1.02	0.75	0.66

(about 3.26 eV at the HSE06 method) agrees well with the report of Zhang *et al.* (about 3.25 eV at the HSE06 method) [16]. For the binary and ternary penta carbides, the electronic band-gap energy ranging from 1.35 to 2.39 eV is found to be lower than that of p-C. This indicates that the substitution of X element with fourfold coordinated C in penta graphene is effective for reducing the band-gap energy. In addition to reducing the band-gap width, the presence of substituted element (Si, Ge, Sn) results in shifting the position of VBM from Γ-X to Γ point of BZ and significantly makes the VBM more dispersed. Moreover, the location of CBM is unchanged for binary carbides and p^1-$X_{0.5}Y_{0.5}$C$_2$ ternary carbides while it moves to the X point for p^2-$X_{0.5}Y_{0.5}$C$_2$ ternary carbides. Since the positions of VBM and CBM are different in the considered paths, the predicted penta carbides are of an indirect band-gap nature. Notably, for the binary penta carbides (p-XC$_2$), the electronic band gap decreases with varying X element in the order of Si > Ge > Sn (i.e., the calculated electronic band gap of p-SiC$_2$, p-GeC$_2$, and p-SnC$_2$ are about 2.39, 2.23, and 1.36 eV, respectively). For the ternary penta carbides, the electronic band gap of p^1-$X_{0.5}Y_{0.5}$C$_2$ is found to be in between that of their corresponding binary counterparts. For instance, the electronic band gap of p^1-Si$_{0.5}$Ge$_{0.5}$C$_2$ about 2.28 eV is in between that of p-SiC$_2$ (2.39 eV) and p-GeC$_2$ (2.23 eV). Moreover, the band gap of p^1-Si$_{0.5}$Ge$_{0.5}$C$_2$ (1.78 eV) is in between that of p-GeC$_2$ (2.23 eV) and p-SnC$_2$ (1.36 eV). However, the electronic structure of p^2-$X_{0.5}Y_{0.5}$C$_2$ with lower band-gap energy is different from p^1-$X_{0.5}Y_{0.5}$C$_2$, revealing that the electronic properties of penta carbides are sensitive to the configuration of alloying elements (X and Y). Thus, the ternary alloying provides the ability to control the electronic properties of penta carbides. We note that there exists a sub-VBM on the Γ to M path for p-C and on the M point for p-XC$_2$ and $p^1 - X_{0.5}Y_{0.5}$C$_2$ penta carbides while the sub-VBM disappeared for p^2-$X_{0.5}Y_{0.5}$C$_2$ penta carbides. We noticed that

there exist some degenerated bands at the valence band region. In order to explain the electronic character of penta carbides, we plotted the pDOS as shown in Fig. 5. According to the pDOS results, the VBM is mainly contributed by p orbitals of X and C atoms, while the CBM dominantly comes from the p_z orbitals of C atoms. The contributions to the electronic states can also be seen from the band decomposed charge density of VBM and CBM (Fig. S5 of the supplemental material [53]). To achieve a better insight into the bonding nature of penta carbides, we analyzed the electron localization function (ELF) [61]. The ELF bonding analysis clearly indicates the σ and π bonds between C=C (Fig. S6 of the supplemental material [53]). Moreover, the X–C (where X = Si, Ge, Sn) bonding in penta carbides is nearly ionic due to the electronegativity difference between X and C atoms.

E. Photocatalytic water-splitting properties

Two-dimensional semiconductors are among the best candidates for photocatalysts [47,62]. To be an efficient photocatalyst for water splitting (to split water into H$_2$ and O$_2$), the following fundamental requirements must be satisfied by semiconductor materials: (1) The band gap must exceed 1.23 eV which is the minimum value of energy demanded to split water into hydrogen and oxygen and (2) the band edges must straddle the redox potentials of water. That is, the location of the VBM must be lower than the oxidation potential of O$_2$/H$_2$O (E_{O_2/H_2O} = -5.67 eV + pH$\times$0.059 eV) and the location of the CBM must be higher than the reduction potential of H$^+$/H$_2$ (E_{H^+/H_2} = -4.44 eV + pH$\times$0.059 eV) so that the reactions become thermodynamically favorable on optical absorption. Penta-carbides with band gap in the range of 1.35 eV to 2.39 eV meet the band-gap requirement for photocatalytic water splitting. To further evaluate their potential as the photocatalyst, we aligned their band edge positions
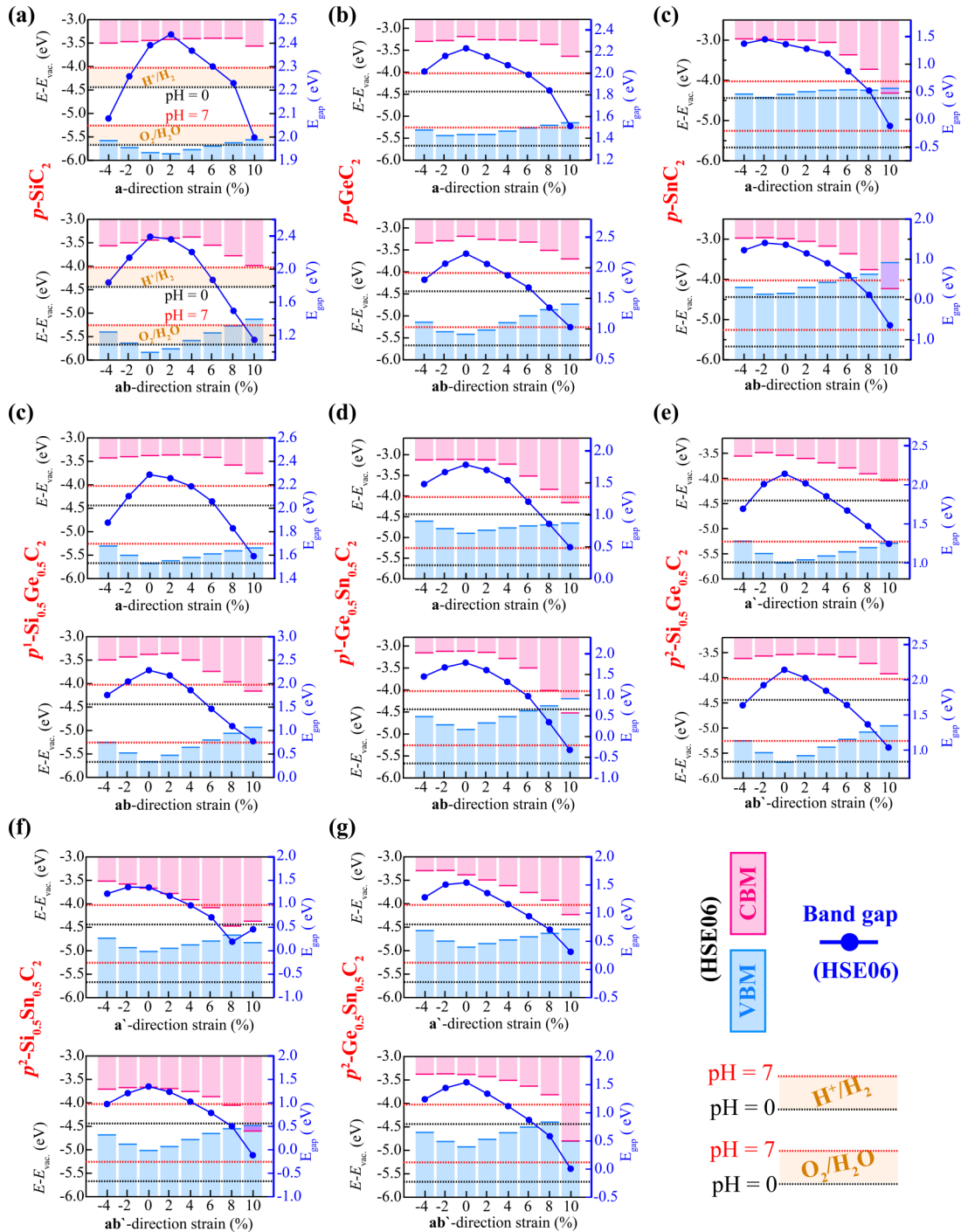
FIG. 8. Variation of band edge positions with respect to the water reduction (H^+/H_2) and oxidation (O_2/H_2O) potentials at pH = 0 and pH = 7 and band-gap energy as a function of uniaxial (upper panels) and biaxial (lower panels) strains for the binary penta carbides (a)–(c) and ternary penta carbides (d)–(g). The vacuum level is set to be zero. Sky blue and pink bars represent the VBM and CBM energies, respectively. The dark blue lines with markers represent the band-gap energy values.

(obtained from the HSE06 hybrid functional) with respect to vacuum level and compared them with the redox potentials for hydrogen and oxygen evolution. The absolute energy value of VBM and CBM for penta carbides is presented in Fig. 6. For p-SiC$_2$, the band edge positions fit perfectly the water reduction and oxidation potentials for overall water splitting in wide pH ranges. For p-GeC$_2$, the energy level of the VBM is above the oxygen evolution reaction (OER) level for water splitting

at pH = 0, but below at the condition of pH = 7, whereas the energy level of the CBM is higher than the hydrogen evolution reaction (HER) for water splitting at both pH = 0 and pH = 7. That is, the CBM and VBM band edges for p-GeC$_2$ satisfy the required redox potential for water splitting at the condition of pH = 7 rather than at pH = 0. Their ternary alloys (p^1-Si$_{0.5}$Ge$_{0.5}$C$_2$ and p^2-Si$_{0.5}$Ge$_{0.5}$C$_2$) fit the redox potentials at both pH = 0 and at pH = 7. Thus, p-SiC$_2$, p-GeC$_2$, and their

ternary alloys are applicable as water splitting photocatalysts. For Sn-based binary and ternary penta carbides, the energy level of CBM is only higher than the reduction potential, indicating that the production of O_2 by water splitting is not appreciable, but the generation of hydrogen can be derived by the large enough reducing power (the energy difference between the VBM and oxidation potential). Besides the above criteria, the efficient separation of photo-induced electron-hole pairs and optical absorption capability are crucial factors for efficient water splitting.

In the view of potential utilization of penta carbides as photocatalysts (and also their applications in nanoelectronics), charge carriers transfer and their spatial separations are essential aspects. The carrier effective mass can give an important information about the ability to transfer electron-hole(s) along specific direction. The effective mass of hole (m_h^*) and electron (m_e^*) in the unit of free electron mass (m_0) are calculated via quadratic fitting of energy (E) band curvature around VBM and CBM as $m_{h/e}^* = \hbar^2[d^2E(k)/dk^2]^{-1}$ where $\hbar$ and k are the reduced Planck constant and wave vector, respectively. We plotted the effective mass of carriers as a function of angle θ in Fig. 7, and the obtained values are listed in Table III. We find that p-C and p-XC$_2$ have the similar shape of angular-dependent carrier effective masses and the carrier effective masses (m_e^* and m_h^*) follow in the order of p-C $> p$-SiC$_2 > p$-GeC$_2 > p$-SnC$_2$. Such that, the existence of X element enhances the carrier transport in penta graphene. The effective mass of hole for p-XC$_2$ binary penta carbides is almost 2–3 times higher than that of electron, suggesting that the transfer of the electron will be faster than that of the holes, and promoting the efficient separation of charge carriers. For p^2-$X_{0.5}Y_{0.5}$C$_2$ ternary penta carbides, the carrier effective masses are much lower than the others. They exhibit strong anisotropic feature. More importantly, the carrier transport in penta graphene can be controlled by binary and ternary alloying of group-IV elements. We should note that as the deformation potential theory is not working well for the materials having nested degenerate bands, here, we did not calculate the carrier mobility of penta carbides.

F. Band-gap and band edge tuning via alloy and strain engineering

Verifying the great distinct stability of the binary and ternary penta carbides, as we have discussed above, alloying provides the ability to tune the electronic properties and tailor the band edge positions. Besides the alloying, we now introduce the strategy to engineer the electronic band gaps of penta carbides by strain. It is known that strain is an effective way to tune the electronic properties of low-dimensional materials [4,47,62,63]. We systematically investigated the electronic properties of penta carbides under uniaxial and isotropic strains. The electronic band gaps and band edges of the binary and ternary penta carbides (calculated by the HSE06 hybrid functional method) are presented in Fig. 8. As is clearly visible, the variation of band gaps of penta carbides under strain conditions are quite similar. In general, the electronic band gaps decrease with increasing compression and tensile strains (uniaxial or biaxial). Notably, the semiconductor (indirect)-to-metal transition takes place when the
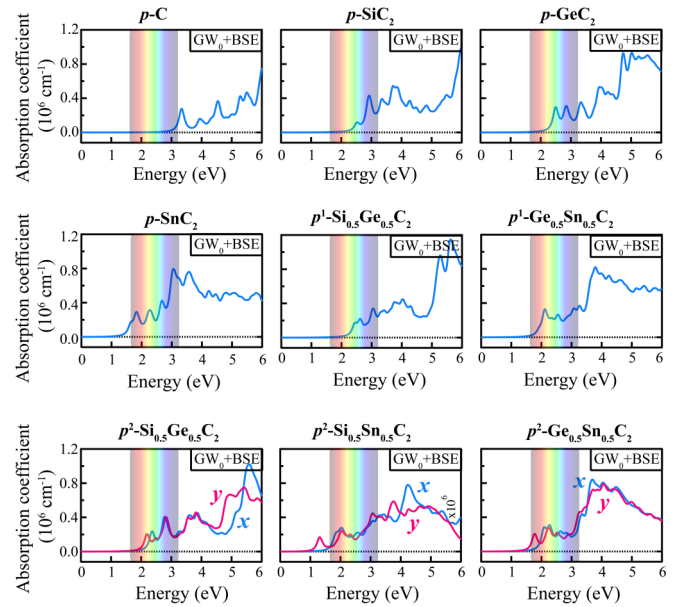

FIG. 9. Calculated optical absorption coefficients for the unitary (p-C), binary (p-XC$_2$), and ternary (p^1-$X_{0.5}Y_{0.5}$C$_2$ and p^2-$X_{0.5}Y_{0.5}$C$_2$) penta carbides using the GW$_0$+BSE method. The color spectrum (inset) represents visible light energy regions.

Sn-based penta cabides are subjected to a large strain ($\sim$10%). Moreover, p^1-Ge$_{0.5}$Sn$_{0.5}$C$_2$ undergoes a transition from an indirect-to-direct band-gap semiconductor for at $\sim$10% strain along the **a** direction. Remarkably, the band edge positions of the strain imposed p-SiC$_2$, p-GeC$_2$, and p^1-Si$_{0.5}$Ge$_{0.5}$C$_2$, and p^2-Si$_{0.5}$Ge$_{0.5}$C$_2$ are also favorable for photocatalytic water splitting.

G. Optical properties

Besides the criteria for photocatalytic water splitting mentioned above, the optical absorption capability is crucial for the efficiency of photocatalytic water splitting. A photocatalyst must have excellent optical absorption, mainly in the visible region to harvest solar energy efficiently. To investigate the optical absorption ability of penta carbides, we calculated the optical absorption coefficient $\alpha(\omega)$ using the following expression;

$$\alpha(\omega) = \sqrt{2}\omega\left\{\sqrt{\varepsilon_1^2(\omega) + \varepsilon_2^2(\omega)} - \varepsilon_1(\omega)\right\}^{\frac{1}{2}}, \quad (8)$$

where $\varepsilon_1(\omega)$ and $\varepsilon_2(\omega)$ are the real and imaginary parts of the frequency-dependent dielectric functions, respectively, which are obtained by solving the Bethe-Salpeter equation (BSE) where the quasiparticle (QP) energies and screened interactions W are obtained by the GW approximation. The calculated $\alpha(\omega)$ of penta carbides with in-plane light polarization using the state-of-the-art GW$_0$ + BSE calculations is presented in Fig. 9. We found that the first absorption peak of p-C is located at 3.42 eV, and the prominent optical absorption peaks are observed at near ultraviolet region. For the binary penta carbides, the absorption peak positions move at lower energy (red shifts) with increasing the atomic number of X element ($X =$ Si, Ge, Sn) in p-XC$_2$. Such that, the first absorption peak of p-SiC$_2$, p-GeC$_2$, and

p-SnC$_2$ appears in the visible region at the energy of 2.52, 2.50, and 1.82 eV, respectively. Remarkably, penta carbides exhibit strong visible light absorption. The optical absorption coefficient can reach up to the order of $\sim 10^5$ cm^{-1} in the visible light region and $\sim 10^6$ cm^{-1} in the ultraviolet region, which is comparable to perovskite solar cells [64], and promising for optoelectronic device applications. Therefore, the strong absorption capability and the wide absorption spectrum within the visible-ultraviolet spectral region suggest that the proposed penta carbides are promising candidates for photocatalytic water splitting.

IV. CONCLUSION

Using the state-of-the-art ab-*initio* calculations, we have explored a series of novel 2D group-IV penta carbides, including C$_2$ dimers and X atoms (X = Si, Ge, Sn). We have ensured the energetic, dynamical, thermal, and mechanical stability of the unitary, binary, and ternary penta carbides. After verifying their great stabilities, we have systematically studied their structural, mechanical, electronic, and optical properties. The lattice dynamics results revealed that penta carbides have a large phononic gap, which can be modulated by hydrogenation and alloy engineering. The alloying offers the ability to tailor the structural, mechanical, and electronic properties of penta carbides. Electronic band structures revealed that penta carbides are indirect semiconductors with band-gap energy ranging from 1.35 eV and 2.39 eV, can be continuously tuned by strain and alloy engineering. Besides the suitable band gaps, the band edge positions of penta carbides (except for Sn-based ones) are suitable for photocatalytic water splitting. They show strong light absorption coefficient within the visible and ultraviolet spectral ranges and the small anisotropic carrier effective masses. The carrier transport in penta graphene can be controlled by alloying of group-IV elements. Taken together, all these results suggest that penta carbides are promising candidates for nanoelectronics and photocatalytic water splitting.

[1] K. S. Novoselov, A. K. Geim, S. V. Morozov, D. Jiang, Y. Zhang, S. V. Dubonos, I. V. Grigorieva, and A. A. Firsov, Science **306**, 666 (2004).

[2] A. K. Geim and K. S. Novoselov, *Nanoscience and Technology: A Collection of Reviews from Nature Journals* (World Scientific, Singapore, 2010), pp. 11–19.

[3] S. Ipek, M. E. Kilic, A. Mogulkoc, S. Cahangirov, and E. Durgun, Phys. Rev. B **98**, 241408(R) (2018).

[4] M. E. Kilic and K.-R. Lee, Nanoscale **13**, 9303 (2021).

[5] S. Cahangirov, M. Topsakal, E. Aktürk, H. Şahin, and S. Ciraci, Phys. Rev. Lett. **102**, 236804 (2009).

[6] B. Feng, Z. Ding, S. Meng, Y. Yao, X. He, P. Cheng, L. Chen, and K. Wu, Nano Lett. **12**, 3507 (2012).

[7] L. Li, S.-Z. Lu, J. Pan, Z. Qin, Y.-Q. Wang, Y. Wang, G.-Y. Cao, S. Du, and H.-J. Gao, Adv. Mater. **26**, 4820 (2014).

[8] L. Zhang, P. Bampoulis, A. N. Rudenko, Q. Yao, A. Van Houselt, B. Poelsema, M. Katsnelson, and H. J. W. Zandvliet, Phys. Rev. Lett. **116**, 256804 (2016).

[9] F.-F. Zhu, W.-J. Chen, Y. Xu, C.-L. Gao, D.-d. Guan, C.-H. Liu, D. Qian, S.-C. Zhang, and J.-F. Jia, Nat. Mater. **14**, 1020 (2015).

[10] Z. Ni, Q. Liu, K. Tang, J. Zheng, J. Zhou, R. Qin, Z. Gao, D. Yu, and J. Lu, Nano Lett. **12**, 113 (2012).

[11] A. Nijamudheen, R. Bhattacharjee, S. Choudhury, and A. Datta, J. Phys. Chem. C **119**, 3802 (2015).

[12] H. Şahin, S. Cahangirov, M. Topsakal, E. Bekaroglu, E. Akturk, R. T. Senger, and S. Ciraci, Phys. Rev. B **80**, 155453 (2009).

[13] P. Zhang, B. B. Xiao, X. L. Hou, Y. F. Zhu, and Q. Jiang, Sci. Rep. **4**, 3821 (2014).

[14] J. Wen Feng, Y. Jie Liu, and J. Xiang Zhao, J. Mol. Graph. Modell. **60**, 132 (2015).

[15] N. Wang, Y. Tian, J. Zhao, and P. Jin, J. Mol. Graph. Modell. **66**, 196 (2016).

[16] S. Zhang, J. Zhou, Q. Wang, X. Chen, Y. Kawazoe, and P. Jena, Proc. Natl. Acad. Sci. USA **112**, 2372 (2015).

[17] J. I. Cerdá, J. Sławińska, G. Le Lay, A. C. Marele, J. M. Gómez-Rodríguez, and M. E. Dávila, Nat. Commun. **7**, 13076 (2016).

[18] G. Prévot, C. Hogan, T. Leoni, R. Bernard, E. Moyen, and L. Masson, Phys. Rev. Lett. **117**, 276102 (2016).

[19] Y. Aierken, O. Leenaerts, and F. M. Peeters, Phys. Chem. Chem. Phys. **18**, 18486 (2016).

[20] Y. Guo, C. Zhang, J. Zhou, Q. Wang, and P. Jena, Phys. Rev. Appl. **11**, 064063 (2019).

[21] Z. Gao, Z. Zhang, G. Liu, and J.-S. Wang, Phys. Chem. Chem. Phys. **21**, 26033 (2019).

[22] X. Li, H. Li, X. Zuo, L. Kang, D. Li, B. Cui, and D. Liu, J. Phys. Chem. C **122**, 21763 (2018).

[23] X. Li, Y. Dai, M. Li, W. Wei, and B. Huang, J. Mater. Chem. A **3**, 24055 (2015).

[24] M. Sternberg, P. Zapol, and L. A. Curtiss, Phys. Rev. B **68**, 205330 (2003).

[25] F. Calvo, S. Diaz-Tendero, and M.-A. Lebeault, Phys. Chem. Chem. Phys. **11**, 6345 (2009).

[26] Q. Wang, M.-F. Ng, S.-W. Yang, Y. Yang, and Y. Chen, Acs Nano **4**, 939 (2010).

[27] J.-O. Joswig and M. Springborg, J. Chem. Phys. **129**, 134311 (2008).

[28] B. Guo, K. Kerns, and A. Castleman, Science **255**, 1411 (1992).

[29] T. Zhao, S. Zhang, Y. Guo, and Q. Wang, Nanoscale **8**, 233 (2016).

[30] T. Zhao, J. Zhou, Q. Wang, Y. Kawazoe, and P. Jena, ACS Appl. Mater. Interfaces **8**, 26207 (2016).

[31] M. E. Kilic and K.-R. Lee, Carbon **181**, 421 (2021).

[32] G. Kresse and J. Hafner, J. Phys.: Condens. Matter **6**, 8245 (1994).

[33] G. Kresse and D. Joubert, Phys. Rev. B **59**, 1758 (1999).

[34] P. E. Blöchl, Phys. Rev. B **50**, 17953 (1994).

[35] J. P. Perdew, K. Burke, and M. Ernzerhof, Phys. Rev. Lett. **77**, 3865 (1996).

[36] H. J. Monkhorst and J. D. Pack, Phys. Rev. B **13**, 5188 (1976).

[37] L. Chaput, A. Togo, I. Tanaka, and G. Hug, Phys. Rev. B **84**, 094302 (2011).

[38] S. Nosé, J. Chem. Phys. **81**, 511 (1984).

[39] S. Nosé, Mol. Phys. **52**, 255 (1984).

[40] W. G. Hoover, Phys. Rev. A **31**, 1695 (1985).

[41] J. Heyd, G. E. Scuseria, and M. Ernzerhof, J. Chem. Phys. **118**, 8207 (2003).

[42] J. Paier, M. Marsman, K. Hummer, G. Kresse, I. C. Gerber, and J. G. Ángyán, J. Chem. Phys. **124**, 154709 (2006).

[43] M. Shishkin and G. Kresse, Phys. Rev. B **74**, 035101 (2006).

[44] F. Karlicky and M. Otyepka, J. Chem. Theory Comput. **9**, 4155 (2013).

[45] D. Fan, S. Lu, Y. Guo, and X. Hu, J. Mater. Chem. C **5**, 3561 (2017).

[46] Y. Li, F. Li, Z. Zhou, and Z. Chen, J. Am. Chem. Soc **133**, 900 (2011).

[47] M. E. Kilic and K.-R. Lee, Carbon **174**, 368 (2021).

[48] G. R. Berdiyorov and M. E.-A. Madjet, RSC Adv. **6**, 50867 (2016).

[49] J. Escudié, C. Couret, and H. Ranaivonjatovo, Coord. Chem. Rev. **178**, 565 (1998).

[50] N. Sathishkumar, S.-Y. Wu, and H.-T. Chen, Chem. Eng. J. **391**, 123577 (2020).

[51] L.-F. Huang, P.-L. Gong, and Z. Zeng, Phys. Rev. B **91**, 205433 (2015).

[52] L. Li, Y. Yu, G. J. Ye, Q. Ge, X. Ou, H. Wu, D. Feng, X. H. Chen, and Y. Zhang, Nat. Nanotechnol. **9**, 372 (2014).

[53] See supplemental material at http://link.aps.org/supplemental/10.1103/PhysRevMaterials.5.065404 for more information on optimized atomic configuration and phonon band structure of p-SiC$_2$H$_2$; phonon instability of p^1-Si$_{0.5}$Sn$_{0.5}$C$_2$; AIMD results for unitary, binary, and ternary penta carbides; strain energy vs strain for uniaxial, biaxial, and shear strains; charge density of the band edges (VBM and CBM); and ELF plot.

[54] M. E. Kilic and K.-R. Lee, Carbon **161**, 71 (2020).

[55] M. E. Kilic and K.-R. Lee, J. Phys. Chem. C **124**, 8225 (2020).

[56] M. Born and K. Huang, *Dynamical Theory of Crystal Lattices* (Oxford University Press, Oxford, 1954).

[57] E. Cadelano, P. L. Palla, S. Giordano, and L. Colombo, Phys. Rev. B **82**, 235414 (2010).

[58] M. Manju, K. Ajith, and M. Valsakumar, Mech. Mater. **120**, 43 (2018).

[59] Q. Peng, C. Liang, W. Ji, and S. De, Mech. Mater. **64**, 135 (2013).

[60] J. Rehman, X. Fan, and W. Zheng, Mater. Today Commun. **26**, 101768 (2020).

[61] A. Savin, R. Nesper, S. Wengert, and T. F. Fässler, Angew. Chem., Int. Ed. Engl. **36**, 1808 (1997).

[62] M. E. Kilic and K.-R. Lee, J. Mater. Chem. C **9**, 4971 (2021).

[63] M. E. Kilic and S. Erkoc, J. Comput. Theor. Nanosci. **10**, 104 (2013).

[64] M. Shirayama, H. Kadowaki, T. Miyadera, T. Sugita, M. Tamakoshi, M. Kato, T. Fujiseki, D. Murata, S. Hara, T. N. Murakami *et al.*, Phys. Rev. Appl. **5**, 014012 (2016).